Journal of Reinforced Plastics and Composites, Vol. 21 Issue 14, Sept. 2002

Radial Elastic Modulus for the Interface between FRP Reinforcing Bars and Concrete

Hailing Yu and James V. Cox
Department of Civil Engineering
Johns Hopkins University
Baltimore, MD 21218

ABSTRACT: The surface structure of reinforcing elements within a matrix can produce a complex mechanical interaction including mechanical interlocking along the interface. This interaction can be modeled using an interface idealization at a scale in which the details of the surface structure are omitted and the actual interface traction is homogenized over a length characteristic of the surface structure. For some applications such as the reinforcement of concrete with FRP bars, the reinforcing element can be idealized as being a circular cylinder, and the radial elastic interaction can affect the overall behavior, e.g. the "bond response" and failure mode of the composite system. The definition of the radial elastic modulus for the interface of the "homogenized model" requires static equivalence of the actual and homogenized tractions and equal amounts of strain energy in the domains. A unit cell approach is taken idealizing the traction distribution as periodic, and an analytical solution for the strain energy in the reinforcing element is presented. The analytical expression for the elastic modulus reflects its dependence upon the traction distribution, material properties, and bar geometry. To study the effects of these parameters, three bond specimens of an FRP bar in a concrete matrix are examined. As the actual traction distribution becomes more concentrated, the interface of the homogenized model becomes more compliant. With respect to material properties, the radial elastic modulus is usually most sensitive to changes in the transverse Young's modulus of the FRP bar; for light weight concrete the modulus is equally sensitive to changes in Young's modulus of the concrete. The elastic moduli are applied to accurately reproduce the effects of a nonuniform traction distribution even when the concrete is split longitudinally and snap-back behavior occurs in the radial response. The traction distribution and compliance of the FRP bar have a significant effect on the snap-back behavior which indicates the potential for a very sudden failure due to concrete cracking.

Key words: surface structure, fiber-reinforced polymer, concrete, transverse isotropy, elastic modulus, interface, homogenization, reinforcement, bond splitting, snap back.

James V. Cox: Dr. Cox is an assistant professor of Civil Engineering at Johns Hopkins University. His research interests are in modeling the mechanical behavior of materials and their interfaces and in computational mechanics. His recent work has focused on understanding and characterizing the mechanical interaction of steel and fiber-reinforced-polymer reinforcing elements with concrete.

Hailing Yu: Ms. Yu is a Ph.D. student in the department of Civil Engineering at Johns Hopkins University. Her research focuses on understanding and characterizing the mechanical interaction along the interface of concrete and FRP/steel reinforcing elements.

1. INTRODUCTION

Interface descriptions of the mechanical interaction between two constituent materials of a body are common in computational mechanics. Often the characterization of this interaction includes an elastic component, which has different interpretations depending upon the application [1] Cox and Yu 1999. In this study, the elastic component is defined to characterize the local elastic response associated with mechanical interlocking between *surface structures*[1], which are not explicitly modeled at a larger scale. Local response has previously been used to argue the need for elastic moduli associated with interface models, and elastic deformation of the contact zone has been experimentally measured for some applications (see e.g., Goodman et al. [2] 1968).

Recently Cox and Yu [1] (1999) derived an analytical expression for the elastic modulus of an interface model characterizing the elastic interaction between a slender axisymmetric reinforcing element and a matrix. For composites having an interphase or imperfect interaction between the two phases, most studies on elastic moduli have sought to determine the effective elastic moduli of an interphase region of finite thickness (see e.g., [3,4]) or to determine the effective elastic moduli of the complete composite (see e.g., [5-10]); however, the study by Cox and Yu [1] (1999) was motivated by the need for computational models at a scale in which the reinforcement and matrix are modeled as solids, and an interface model is used to characterize the progressive failure of the mechanical interaction. That initial study and the study presented in this paper address the radial (normal) component of the elastic interaction, but the approach could also be used to examine the increased tangent compliance along a material interface due to imperfect interaction.

Like the earlier study [1] (1999), the research presented in this study may be applicable to different composite materials or structures, but the two studies differ in the motivating problem. In the previous study, the deformation of the reinforcement was neglected, thus the formulation was limited to composites with reinforcing elements (e.g. steel) having a small transverse compliance relative to the matrix (e.g. concrete). In this study, the motivating problem (for which the theory is demonstrated) is the mechanical interaction between fiber-reinforced polymer (FRP) reinforcing bars and a concrete matrix. For FRP bars the transverse compliance is approximately 20 to 30 times that of steel and approximately 2 to 4 times that of concrete, thus the local deformation of both the matrix and reinforcement are now considered. Similar to steel bars, many FRP bars have a fabricated surface structure (often idealized as being periodic) that produces a significant mechanical interlocking with the adjacent concrete (after the propagation of an interfacial crack). The mechanical interlocking produces a complicated interface traction distribution due to the resulting contact conditions. The radial component of the traction tends to produce significant hoop stress in the adjacent concrete and can fail the concrete in longitudinal cracking[2] (see e.g., Tepfers [11]1979). The increased radial compliance of the FRP bars affects the mechanical interlocking. Figure 1 shows the bond stress *vs*. slip response for a recent pull-out test of an FRP bar. This type of "cyclic behavior" has been observed for several bond tests of FRP bars (see e.g., [12]). The spatial period of the response cycles corresponds to the length of the periodic surface structure of the bar, reflecting the importance of the mechanical interlocking and that there must be significant radial compliance. The increase in radial

---

[1] *Surface structure* refers to the deviation of the actual geometry from that of an idealized model. For example, an idealized model might represent a reinforcing element as a circular cylinder. The surface structure in this case would be the portion of the actual reinforcing element that deviates from the cylindrical shape. The surface structure is referred to as being *significant* if it produces significant mechanical interlocking when relative slip occurs along the interface.

[2] Ideal longitudinal cracks occur in a θ-plane assuming a cylindrical coordinate system in which the z-axis is aligned with the axis of the bar.

compliance has been associated with the elastic properties of the FRP, but the effect of the contact conditions has not been examined.

One motivation for examining the radial compliance is that it can significantly affect the bond strength and failure mode for an FRP bar in a concrete matrix (pull-out *vs*. failure due to longitudinal cracking – *splitting failure*). For computational "bond models" in which the surface structure geometry is explicitly modeled (*rib-scale* models [13](Cox and Herrmann 1998)) the detailed effects of the mechanical interlocking are accounted for directly. While this scale of modeling is useful for understanding the mechanisms that contribute to bond behavior, it is impractical for the analysis of structural components. A larger scale of modeling (*bar scale* [13] (Cox and Herrmann 1998)) amenable to the analysis of structural components represents the reinforcement as an cylindrical solid (eliminating the geometric detail of the surface structure) and uses an interface idealization to characterize the effects of mechanical interlocking. This type of model was recently used by Guo and Cox [14,15] (1998, 1999) to reproduce the behavior of various test specimens. The model represents the kinematics of the mechanical interlocking (i.e., the "wedging effect" of the surface structure) through an inelastic radial dilation of the interface which is partially negated by an elastic radial contraction of the interface (representing the local elastic deformation). Unfortunately while the tangent elastic response can be estimated from experimental data, experimental data on the radial elastic response is not available. Thus further investigation of the radial elastic modulus associated with the interface is needed.

This paper focuses on the radial elastic response attributed to an interface idealization when the actual traction distribution along the interface is assumed to be axisymmetric and nonuniform (but periodic) in the axial direction. While the actual traction distribution will not generally satisfy these assumptions, these idealizations can allow analytical results to be obtained that yield significant insight. Furthermore, the analytical solution can be applied as a first order approximation when these assumptions are not strictly true.

The paper is organized in sections that address the following areas: (2) simplifications that lead to the underlying analytical models needed to define the elastic modulus of the interface, (3) analytical solution and verification, (4) use of the analytical solution to determine an equivalent elastic modulus of the interface idealization and presentation of parameter study results, (5) application of the model in predicting longitudinal cracking in a concrete matrix, and (6) summary and conclusions.

2. ANALYTICAL MODEL

To define an elastic modulus for an interface idealization that incorporates analytical solutions, a few simplifications are adopted at both scales (rib-scale and bar-scale). At both scales the interface is idealized as being smooth, eliminating the details of the actual surface structure geometry, but not the effects of the mechanical interlocking caused by the geometry. At the smaller scale (rib-scale), the effect of mechanical interlocking is represented by a more concentrated interfacial traction distribution. This differs with a typical computational rib-scale model where the geometry is explicitly modeled. (It was previously found for a steel bond specimen that the effect of traction distribution is more significant than the effect of the actual geometry [1] (1999).) For the bar-scale model the actual traction is homogenized over a characteristic length, e.g., the length of spatial periodicity of the surface structure. By definition, the actual and homogenized tractions are statically equivalent loads, but their mechanical effects differ. The following analysis will show that the uniform traction produces a stiffer load-deflection response for the interface than the actual traction distribution does. To capture the added compliance caused by the actual traction distribution, a finite elastic modulus is attributed to the interface of the bar-scale model.

Figures 2(a-d) show θ-sections of the axisymmetric rib- and bar-scale models. The concrete is modeled as a thick-walled cylinder and idealized as being homogeneous, isotropic and linear elastic (Young's modulus E_c and Poisson's ratio ν_c). The FRP cylinder is treated as transversely

isotropic and linear elastic with five independent material constants: longitudinal Young's modulus (E_L), transverse Young's modulus (E_T) and Poisson's ratio (ν_{TT}), and longitudinal-transverse shear modulus (μ_{LT}) and Poisson's ratio (ν_{LT}).

Let s_r denote the characteristic length associated with the assumed periodic structure (e.g., rib-spacing) along the longitudinal axis (z-axis). In Figures 2(a-d) the elastic problems are defined for a unit cell of length s_r. The rollers along the edges $z=\pm s_r/2$ and the radial traction distributions (even about the r-axis) produce response symmetries consistent with the unit cell assumptions. For the rib-scale model (Figures 2a,c) the radial traction distribution t is nonzero over the contact length L_t, and for the bar-scale model (Figures 2b,d) σ denotes the homogenized traction over s_r. The tractions are related through static equivalence as

$$\sigma = \frac{1}{s_r}\int_{-s_r/2}^{s_r/2} t(z)dz \tag{1}$$

The interface model for the bar-scale problem has a *radial elastic stiffness* (denoted as D^e) that relates σ to the relative radial displacement (δ_n) of initially coincident points on the interface (positive in extension). The radial elastic stiffness of the interface (for brevity, the *interface stiffness*) has dimensions of force per length^3. Alternatively, deformations of the interface are often nondimensionalized by characteristic lengths that can be related to the surface structure (see e.g., [13,16]); thus some results will be presented in terms of a generalized strain measure defined as

$$q_n = \delta_n / d_b \tag{2}$$

where $d_b=2r_i$, the bar diameter. (The surface structure scales with d_b for typical FRP bars.) The corresponding *radial elastic modulus* relating σ and q_n is denoted by $\hat{D}^e$. Thus σ is related to the interface stiffness, elastic modulus and kinematic variables by

$$\sigma = D^e \delta_n = \hat{D}^e q_n \tag{3a}$$

where

$$D^e = \hat{D}^e / d_b \tag{3b}$$

The increase in compliance associated with the concentration of the actual interface traction can be additively decomposed into parts associated with the concrete ($1/D^e_{con}$, Figure 2b) and reinforcing bar ($1/D^e_{bar}$, Figure 2d); i.e., the interface compliance satisfies

$$D^{e\,-1} = D^{e\,-1}_{con} + D^{e\,-1}_{bar} \tag{4a}$$

similarly

$$\hat{D}^{e\,-1} = \hat{D}^{e\,-1}_{con} + \hat{D}^{e\,-1}_{bar} \tag{4b}$$

By Equation (1) the rib- and bar-scale models are equivalent in the Saint-Venant sense. Further, we equate the strain energies stored in the elastic bodies of problems (a,c) to those of problems (b,d). We select this equivalence measure because potentially the strain energy can be released to drive cracks in the materials. Since the strain energy stored in an elastic body is equal to the work done by external loading, the "energy equivalence" requires

$$W^t_a = W^\sigma_b \qquad\qquad W^t_c = W^\sigma_d \tag{5a,b}$$

where W^t_a denotes the work done by t in problem (a), and so on. Solving expressions for the elastic modulus from Equations (4) and (5) requires the work done by the tractions upon each of the four subdomains (Figure 2) to be obtained analytically. The next section addresses the analytical solutions to these elasticity problems.

3. ANALYTICAL SOLUTION

The solutions associated with the "exterior parts" of the problems (Figures 2a and 2b) were previously presented [1]. This section complements the previous work with the solution for a transversely isotropic cylindrical bar loaded as depicted in Figure 2c.

3.1 Governing Equations and Boundary Conditions

The governing equations for the axisymmetric problem are as follows. Equilibrium is governed by

$$\frac{\partial \sigma_{rr}}{\partial r}+\frac{\partial \sigma_{rz}}{\partial z}+\frac{\sigma_{rr}-\sigma_{\theta\theta}}{r}=0, \qquad \frac{\partial \sigma_{rz}}{\partial r}+\frac{\partial \sigma_{zz}}{\partial z}+\frac{\sigma_{rz}}{r}=0, \tag{6a,b}$$

and $\sigma_{r\theta}=\sigma_{\theta z}=0$. The linear strain-displacement relationships are

$$\varepsilon_{rr}=\frac{\partial u_r}{\partial r}, \qquad \varepsilon_{\theta\theta}=\frac{u_r}{r}, \qquad \varepsilon_{zz}=\frac{\partial u_z}{\partial z}, \qquad \gamma_{rz}=\frac{\partial u_r}{\partial z}+\frac{\partial u_z}{\partial r}, \tag{7a-d}$$

and $\gamma_{r\theta}=\gamma_{\theta z}=0$. The constitutive relationships for linear transversely isotropic elasticity can be written as

$$\sigma_{rr}=C_{11}\varepsilon_{rr}+C_{12}\varepsilon_{\theta\theta}+C_{13}\varepsilon_{zz}, \qquad \sigma_{\theta\theta}=C_{12}\varepsilon_{rr}+C_{11}\varepsilon_{\theta\theta}+C_{13}\varepsilon_{zz}, \tag{8a,b}$$

$$\sigma_{zz}=C_{13}\varepsilon_{rr}+C_{13}\varepsilon_{\theta\theta}+C_{33}\varepsilon_{zz}, \qquad \sigma_{rz}=C_{44}\gamma_{rz}, \tag{8c,d}$$

where

$$C_{11}=E_{\mathrm{T}}(-E_{\mathrm{L}}+E_{\mathrm{T}}\nu_{\mathrm{LT}}^2)/\Lambda, \qquad C_{12}=-E_{\mathrm{T}}(E_{\mathrm{L}}\nu_{\mathrm{TT}}+E_{\mathrm{T}}\nu_{\mathrm{LT}}^2)/\Lambda,$$

$$C_{13}=-E_{\mathrm{L}}E_{\mathrm{T}}\nu_{\mathrm{LT}}(1+\nu_{\mathrm{TT}})/\Lambda, \qquad C_{33}=-E_{\mathrm{L}}^2(1-\nu_{\mathrm{TT}}^2)/\Lambda, \qquad C_{44}=\mu_{\mathrm{LT}}=\mu_{\mathrm{TL}},$$

$$\Lambda=\left[2E_{\mathrm{T}}\nu_{\mathrm{LT}}^2-E_{\mathrm{L}}(1-\nu_{\mathrm{TT}})\right](1+\nu_{\mathrm{TT}}).$$

The solution for an isotropic medium will be included as a special case.

The periodic boundary conditions are given by

$$u_z\big|_{z=\pm s_{\mathrm{r}}/2}=0, \qquad \sigma_{rz}\big|_{z=\pm s_{\mathrm{r}}/2}=0, \tag{9a,b}$$

and the traction boundary conditions on the bar surface are

$$\sigma_{rr}\big|_{r=r_{\mathrm{i}}}=t, \qquad \sigma_{rz}\big|_{r=r_{\mathrm{i}}}=0, \tag{9c,d}$$

where t denotes a generic distribution of traction normal to the surface.

3.2 Solution

The solution approach will be the same as that previously used for the exterior part of the problem [1]Cox and Yu [1999], where the variations of the displacements in the z-direction are expressed in terms of the orthonormal trigonometric basis (i.e. a Fourier series approach). Another common approach is the stress function method which solves a biharmonic equation for the stress function and expresses all the solution variables in terms of this particular function (see e.g., [17][1995]). Pagano ref.?

The trigonometric functions used as the orthonormal basis in the Fourier series are defined as

$$\Phi_{cn}(z)=\begin{cases}\dfrac{1}{\sqrt{s_{\mathrm{r}}}}, & n=0\\[2ex] \dfrac{\cos(z\omega_n)}{\sqrt{s_{\mathrm{r}}/2}}, & n>0\end{cases}, \qquad \Phi_{sn}(z)=\frac{\sin(z\omega_n)}{\sqrt{s_{\mathrm{r}}/2}}, \qquad \omega_n=\frac{2\pi n}{s_{\mathrm{r}}}. \tag{10a-c}$$

Due to the symmetry of the problem, the nonzero displacements u_r and u_z are even and odd functions of z, respectively, and thus can be expressed as

$$u_r(r,z)=\sum_{n=0}^{\infty}v_{rn}(r)\Phi_{cn}(z), \qquad u_z(r,z)=\sum_{n=1}^{\infty}v_{zn}(r)\Phi_{sn}(z). \tag{11a,b}$$

Substituting the above definitions into the strain-displacement and constitutive relationships yields the stress components as

$$\sigma_{rr}(r,z)=\sum_{n=0}^{\infty}\sigma_n(r)\Phi_{cn}(z), \qquad \sigma_{rz}(r,z)=\sum_{n=1}^{\infty}\tau_n(r)\Phi_{sn}(z), \tag{12a,b}$$

where

$$\sigma_0(r) = C_{11}\frac{dv_{r0}}{dr} + C_{12}\frac{v_{r0}}{r}, \tag{13a}$$

$$\sigma_n(r) = C_{11}\frac{dv_{rn}}{dr} + C_{12}\frac{v_{rn}}{r} + C_{13}\omega_n v_{zn}, \qquad \tau_n(r) = C_{44}\left(\frac{dv_{zn}}{dr} - \omega_n v_{rn}\right). \tag{13b,c}$$

Note that the periodic boundary conditions (9a,b) are identically satisfied by Equations (11b, 12b).

The coefficient functions are projections of the solutions onto each basis function, *e.g.*,

$$v_{rn}(r) = \langle u_r(r,z), \Phi_{cn}(z)\rangle, \qquad v_{zn}(r) = \langle u_z(r,z), \Phi_{sn}(z)\rangle \tag{14a,b}$$

where $\langle a,b\rangle = \int_{-s_r/2}^{s_r/2} abdz$. The equations for deriving the coefficient functions can be obtained by projecting the equilibrium equations onto the basis. Orthogonality of the basis functions yields two nontrivial equations

$$\left\langle \Phi_{cn}, \frac{\partial\sigma_{rr}}{\partial r} + \frac{\partial\sigma_{rz}}{\partial z} + \frac{\sigma_{rr}-\sigma_{\theta\theta}}{r}\right\rangle = 0, \qquad \left\langle \Phi_{sn}, \frac{\partial\sigma_{rz}}{\partial r} + \frac{\partial\sigma_{zz}}{\partial z} + \frac{\sigma_{rz}}{r}\right\rangle = 0 \tag{15a,b}$$

The traction boundary conditions (9c,d) are also projected onto the basis

$$\langle \Phi_{cn}, \sigma_{rr}\rangle\big|_{r=r_i} = \langle \Phi_{cn}, t\rangle = \alpha_n, \qquad \langle \Phi_{sn}, \sigma_{rz}\rangle\big|_{r=r_i} = 0, \tag{16a,b}$$

where the α's are the coordinates of t in the Φ_c basis (i.e., Fourier coefficients of t).

For the case of n=0, Equation (15a) gives

$$\frac{d^2v_{r0}}{dr^2} + \frac{1}{r}\frac{dv_{r0}}{dr} - \frac{v_{r0}}{r^2} = 0 \tag{17}$$

whose general solution is a linear combination of r and $1/r$. The term $1/r$ is eliminated due to its singularity at r=0. The solution to v_{r0} is then written as

$$v_{r0}(r) = c_0 r \tag{18a}$$

where c_0 is a constant to be defined. Substituting v_{r0} into Equation (13a) gives the following solution to $\sigma_0(r)$

$$\sigma_0(r) = (C_{11} + C_{12})c_0 \tag{18b}$$

By enforcing the traction boundary condition (16a) for n=0, c_0 is readily solved as

$$c_0 = \alpha_0 / (C_{11}+C_{12}) \tag{18c}$$

The coefficient functions given by Equations (18a,b) multiplied by Φ_{c0} are the displacement and stress solutions corresponding to a uniform traction σ acting over s_r. To later assess the relative magnitude of $\hat{D}^e$, a measure of the transverse stiffness of the bar subjected to a uniform traction ($\hat{D}^T_{bar}$) is calculated as

$$\hat{D}^T_{bar} = \frac{\sigma_0(r_i)\Phi_{c0}}{v_{r0}(r_i)\Phi_{c0}/d_b} = 2(C_{11}+C_{12}) \tag{19}$$

For the case of n>0, Equations (15a,b) lead to the following set of coupled ordinary differential equations for v_{rn} and v_{zn}

$$C_{11}\left(\frac{d^2v_{rn}}{dr^2} + \frac{dv_{rn}}{rdr} - \frac{v_{rn}}{r^2}\right) - \omega_n^2 C_{44}v_{rn} + (C_{13}+C_{44})\omega_n\frac{dv_{zn}}{dr} = 0 \tag{20a}$$

$$-\omega_n(C_{13}+C_{44})\left(\frac{dv_{rn}}{dr} + \frac{v_{rn}}{r}\right) + C_{44}\left(\frac{d^2v_{zn}}{dr^2} + \frac{dv_{zn}}{rdr}\right) - \omega_n^2 C_{33}v_{zn} = 0 \tag{20b}$$

Uncoupling Equations (20a,b) gives the following expression for v_{rn} in terms of a third-order differential operation on v_{zn}

$$v_{rn} = \left[\frac{C_{11}}{\omega_n^3 (C_{13}+C_{44})} \left(\frac{d^3}{dr^3} + \frac{d^2}{rdr^2} - \frac{d}{r^2 dr} \right) - \frac{C_{11}C_{33} - (C_{13}+C_{44})^2}{\omega_n C_{44}(C_{13}+C_{44})} \frac{d}{dr} \right] v_{zn} \tag{21}$$

Substituting Equation (21) back into Equation (20b) gives the fourth order homogeneous differential equation for v_{zn}

$$\left[\left(\frac{d^2}{dr^2} + \frac{d}{rdr} \right)^2 - (p^2+q^2)\omega_n^2 \left(\frac{d^2}{dr^2} + \frac{d}{rdr} \right) + p^2 q^2 \omega_n^4 \right] v_{zn} = 0 \tag{22}$$

where p^2 and q^2 satisfy the following relationships

$$p^2 + q^2 = \frac{C_{11}C_{33} + C_{44}^2 - (C_{13}+C_{44})^2}{C_{11}C_{44}}, \qquad p^2 q^2 = \frac{C_{33}}{C_{11}}. \tag{23a,b}$$

This is equivalent to identifying p^2 and q^2 as the roots to the quadratic algebraic equation

$$(\cdot)^2 - \frac{C_{11}C_{33} + C_{44}^2 - (C_{13}+C_{44})^2}{C_{11}C_{44}} (\cdot) + \frac{C_{33}}{C_{11}} = 0 \tag{23c}$$

The quantities p^2 and q^2 are dimensionless functions of the material constants and are treated as real and positive for this problem.

Equation (22) can be rewritten as

$$(L - p^2\omega_n^2)(L - q^2\omega_n^2) v_{zn} = 0 \tag{24a}$$

where

$$L \equiv \frac{d^2}{dr^2} + \frac{d}{rdr} \tag{24b}$$

Both of the operators in Equation (24a) are scaled, modified Bessel operators of order 0. The solution of v_{zn} depends on the values of p^2 and q^2. In the following two subsections, the cases of distinct ($p^2 \neq q^2$) and identical roots ($p^2 = q^2$) are considered separately.

3.2.1 Case I: $p^2 \neq q^2$

For the case of distinct roots, the general solution to Equation (24a) is a linear combination of the eigenfunctions of the linear operator L corresponding to the two eigenvalues $p^2\omega_n^2$ and $q^2\omega_n^2$. There are four such eigenfunctions, *i.e.* $I_0(p\omega_n r)$, $K_0(p\omega_n r)$, $I_0(q\omega_n r)$ and $K_0(q\omega_n r)$, where I and K denote modified Bessel functions of the first and second kinds, respectively. The terms involving K_0 are eliminated due to their singularity at $r=0$, and the solutions to the displacement coefficient functions are

$$v_{rn}(r) = \eta_p c_{pn} I_1(p\omega_n r) + \eta_q c_{qn} I_1(q\omega_n r), \qquad v_{zn}(r) = c_{pn} I_0(p\omega_n r) + c_{qn} I_0(q\omega_n r) \tag{25a,b}$$

where c_{pn} and c_{qn} are constants, and

$$\eta_p = \frac{pC_{44} - p^{-1}C_{33}}{C_{13}+C_{44}}, \qquad \eta_q = \frac{qC_{44} - q^{-1}C_{33}}{C_{13}+C_{44}} \tag{26a,b}$$

are nondimensional and related to the material constants. Substituting Equations (25a,b) into Equations (13b,c) gives the following coefficient functions for the stress components

$$\sigma_n(r) = c_{pn}\sigma_{c_{pn}}(r) + c_{qn}\sigma_{c_{qn}}(r), \qquad \tau_n(r) = c_{pn}\tau_{c_{pn}}(r) + c_{qn}\tau_{c_{qn}}(r) \tag{27a,b}$$

where

$$\sigma_{c_{pn}}(r) = (C_{11}p\eta_p + C_{13})\omega_n I_0(p\omega_n r) + (C_{12} - C_{11})\eta_p r^{-1} I_1(p\omega_n r), \tag{28a}$$

$$\sigma_{c_{qn}}(r) = (C_{11}q\eta_q + C_{13})\omega_n I_0(q\omega_n r) + (C_{12} - C_{11})\eta_q r^{-1} I_1(q\omega_n r), \tag{28b}$$

$$\tau_{c_{pn}}(r) = (p - \eta_p)\omega_n C_{44} I_1(p\omega_n r), \qquad \tau_{c_{qn}}(r) = (q - \eta_q)\omega_n C_{44} I_1(q\omega_n r) \tag{28c,d}$$

Enforcing the traction boundary conditions (16a,b) yields the following system of equations

$$\begin{bmatrix} \sigma_{c_{pn}}\big|_{r=r_i} & \sigma_{c_{qn}}\big|_{r=r_i} \\ \tau_{c_{pn}}\big|_{r=r_i} & \tau_{c_{qn}}\big|_{r=r_i} \end{bmatrix} \begin{Bmatrix} c_{pn} \\ c_{qn} \end{Bmatrix} = \begin{Bmatrix} \alpha_n \\ 0 \end{Bmatrix} \tag{29}$$

from which the solutions for c_{pn} and c_{qn} are given by

$$c_{pn}=r_i\alpha_n(\eta_q-q)I_1(q\omega_n r_i)/B_n, \qquad c_{qn}=r_i\alpha_n(-\eta_p+p)\,I_1(p\omega_n r_i)/B_n \tag{30a,b}$$

where

$$B_n=\omega_n r_i(-\eta_p+p)(C_{13}+C_{11}q\eta_q)I_0(q\omega_n r_i)I_1(p\omega_n r_i)+\omega_n r_i(\eta_q-q)(C_{13}+C_{11}p\eta_p)I_0(p\omega_n r_i)I_1(q\omega_n r_i)+ (q\eta_p-p\eta_q)(C_{11}-C_{12})I_1(p\omega_n r_i)I_1(q\omega_n r_i) \tag{31}$$

has units of Young's modulus. With these constants, the solutions for the displacement and stress components are complete.

3.2.2 Case II: $p^2=q^2$

For the case of identical roots, Equation (24a) becomes

$$(L-p^2\omega_n^2)^2 v_{zn}=0 \tag{32}$$

The general solution to this equation contains four terms: $I_0(p\omega_n r)$, $K_0(p\omega_n r)$, $p\omega_n r I_1(p\omega_n r)$ and $p\omega_n r K_1(p\omega_n r)$. Again to avoid singularity at $r=0$, we retain only the "I terms." The solution to v_{zn} is then written as

$$v_{zn}(r)=c_{1n}I_0(p\omega_n r)+c_{3n}p\omega_n r I_1(p\omega_n r) \tag{33}$$

where c_{1n} and c_{3n} are unknown constants.

The principal physical problem of interest for this case is material isotropy, which corresponds to $p^2=q^2=1$ mathematically. In this case, the coefficient functions have the same general forms as those for the hollow cylinder problem [1] (see Cox and Yu [1999]), but the boundary conditions lead to different solutions. The solutions are given as follows

$$v_{rn}(r)=-c_{1n}I_1(\omega_n r)+c_{3n}\left[4(1-\nu)I_1(\omega_n r)-\omega_n r I_0(\omega_n r)\right] \tag{34a}$$

$$v_{zn}(r)=c_{1n}I_0(\omega_n r)+c_{3n}\omega_n r I_1(\omega_n r) \tag{34b}$$

$$\sigma_n(r)=2\mu\left[\sigma_{c_{1n}}(r)c_{1n}+\sigma_{c_{3n}}(r)c_{3n}\right], \qquad \tau_n(r)=2\mu\left[\tau_{c_{1n}}(r)c_{1n}+\tau_{c_{3n}}(r)c_{3n}\right] \tag{34c,d}$$

where μ and ν are the shear modulus and Poisson's ratio, respectively, for the isotropic elastic cylinder and

$$\sigma_{c_{1n}}(r)=-\omega_n I_0(\omega_n r)+I_1(\omega_n r)/r, \tag{35a}$$

$$\sigma_{c_{3n}}(r)=(3-2\nu)\omega_n I_0(\omega_n r)-4(1-\nu)I_1(\omega_n r)/r-\omega_n^2 r I_1(\omega_n r) \tag{35b}$$

$$\tau_{c_{1n}}(r)=\omega_n I_1(\omega_n r), \qquad \tau_{c_{3n}}(r)=\omega_n^2 r I_0(\omega_n r)-2(1-\nu)\omega_n I_1(\omega_n r) \tag{35c,d}$$

Enforcing the traction boundary conditions (16a,b) yields the following system of equations for c_{1n} and c_{3n}

$$\begin{bmatrix} \sigma_{c_{1n}}\big|_{r=r_i} & \sigma_{c_{3n}}\big|_{r=r_i} \\ \tau_{c_{1n}}\big|_{r=r_i} & \tau_{c_{3n}}\big|_{r=r_i} \end{bmatrix} \begin{Bmatrix} c_{1n} \\ c_{3n} \end{Bmatrix} = \begin{Bmatrix} \alpha_n/2\mu \\ 0 \end{Bmatrix} \tag{36}$$

which yield

$$c_{1n}=-\alpha_n r_i\left[\omega_n r_i I_0(\omega_n r_i)-2(1-\nu)I_1(\omega_n r_i)\right]/(2\mu F_n) \tag{37a}$$

$$c_{3n}=\alpha_n r_i I_1(\omega_n r_i)/(2\mu F_n) \tag{37b}$$

where

$$F_n=\omega_n^2 r_i^2\left[I_0^2(\omega_n r_i)-I_1^2(\omega_n r_i)\right]-2(1-\nu)I_1^2(\omega_n r_i) \tag{38}$$

3.3 Verification

To verify the mathematical form of the elastic solutions, the analytical results for a unit cell of an FRP bar are compared with the results obtained from a finite element analysis. The unit cell

corresponds to the "type D" GFRP bar used in the bond tests of Malvar [18,19] (1994,1995). The geometric parameters are listed in Table 1 (specimen a). The transverse isotropic material constants were estimated by Guo and Cox [14] using approximate formulae of Hashin [20]. The analysis assumptions associated with the contact are: (1) the contact length (L_t) is $s_r/8$, and (2) t is compressive and uniformly distributed over L_t with a magnitude of 8 MPa, corresponding to σ=-1 MPa.

Figure 3 compares the displacement solutions (u_r and u_z) along the r and z directions. Two analytical results using 20 and 40 terms in the series expansions are shown to indicate the extent of convergence. The finite element solution used 336 bilinear quadrilateral elements graded more finely near the applied traction. The good agreement of these three results suggests that the analytical solution is correct.

4. ELASTIC MODULUS

With the elastic solutions, now we can compute the work expressions needed in Equations (5) and derive a closed-form expression for $\hat{D}^e$. The analytical expression provides a convenient means of studying the dependence of $\hat{D}^e$ on various parameters.

4.1 Formulation

The work done by t in problem c (Figure 2c) can be calculated as follows

$$W_c^t = \int_{-s_r/2}^{s_r/2} \tfrac{1}{2}\left[2\pi r_i t(z)\right] u_r^{bar}(r_i, z)dz = \pi r_i \sum_{n=0}^{\infty} \alpha_n v_{rn}^{bar}(r_i) = W_0^{bar} + \pi r_i \sum_{n=1}^{\infty} \alpha_n v_{rn}^{bar}(r_i) \tag{39a}$$

where the superscript "bar" denotes the bar subdomain, α_n and $v_{rn}(r_i)$ are the Fourier coefficients of t and $u_r(r_i,z)$, respectively, and $W_0=\pi r_i \alpha_0 v_{r0}(r_i)$ is the work done by a uniformly distributed radial traction σ acting over s_r. In a similar manner, applying the elastic solution for the concrete subdomain (Cox and Yu [1999]) [1] and the definitions of Equations (2,3a), we can explicitly write the other work terms of Equations (5) as

$$W_a^t = W_0^{con} - \pi r_i \sum_{n=1}^{\infty} \alpha_n v_{rn}^{con}(r_i) \tag{39b}$$

$$W_b^\sigma = W_0^{con} + \pi r_i s_r \sigma^2 d_b / \hat{D}_{con}^e, \qquad W_d^\sigma = W_0^{bar} + \pi r_i s_r \sigma^2 d_b / \hat{D}_{bar}^e \tag{39c,d}$$

where $d_b=2r_i$ and the superscript "con" denotes concrete. Substituting Equations (39a-d) into Equations (4b) and (5) and solving for $\hat{D}^e$ gives

$$\hat{D}^e = s_r \sigma^2 d_b \left\{ \sum_{n=1}^{\infty} \alpha_n \left[-v_{rn}^{con}(r_i) + v_{rn}^{bar}(r_i) \right] \right\}^{-1} \tag{40}$$

Cox and Yu [1999] [1] gave $\hat{D}_{con}^e$ for the case of "r_o sufficiently large relative to r_i" (e.g. $r_o/r_i \geq 2$) as follows

$$\hat{D}_{con}^e = \left(\sum_{n=1}^{\infty} -\frac{\alpha_n^2 \kappa_n}{\alpha_0^2 E_c} \right)^{-1} \tag{41}$$

where

$$\kappa_n = \left(1-\nu_c^2\right) K_1^2(\omega_n r_i) \Big/ \left\{ (\omega_n r_i)^2 \left[K_0^2(\omega_n r_i) - K_1^2(\omega_n r_i) \right] - 2\left(1-\nu_c\right) K_1^2(\omega_n r_i) \right\} \tag{42}$$

is nondimensional. (Note: The relationship $\sigma=\alpha_0/\sqrt{s_r}$ is employed in the derivation of $\hat{D}_{con}^e$.)

For $\hat{D}_{bar}^e$ the cases with transversely isotropic (FRP) and isotropic (steel) bars are considered separately.

4.1.1 Transversely Isotropic Bars – FRP Bar Case

Based on the *Case I* solutions (section 3.2.1) and Equation (40), the radial elastic modulus of the interface for an FRP bar is

$$\hat{D}^{\mathrm{e}}_{\mathrm{bar}} = \left(\sum_{n=1}^{\infty} \frac{\alpha_n^2 \xi_n}{\alpha_0^2 B_n} \right)^{-1} \tag{43}$$

where B_n is given by Equation (31), and ξ_n is dimensionless and given by

$$\xi_n = \tfrac{1}{2} \left(p\eta_q - q\eta_p \right) J_1(p\omega_n r_{\mathrm{i}}) J_1(q\omega_n r_{\mathrm{i}}) \tag{44}$$

The radial elastic modulus accounting for both contributions can then be written as

$$\hat{D}^{\mathrm{e}} = \left(\hat{D}^{\mathrm{e}}_{\mathrm{con}}{}^{-1} + \hat{D}^{\mathrm{e}}_{\mathrm{bar}}{}^{-1} \right)^{-1} = \left[\sum_{n=1}^{\infty} \frac{\alpha_n^2}{\alpha_0^2} \left(\frac{\xi_n}{B_n} - \frac{\kappa_n}{E_{\mathrm{c}}} \right) \right]^{-1} \tag{45}$$

$\hat{D}^{\mathrm{e}}$ is dependent on the traction distribution (via α_n/α_0), the seven independent material constants of the FRP and concrete (i.e., E_{L}, E_{T}, μ_{LT}, ν_{LT}, ν_{TT}, E_{c} and ν_{c}) and $r_{\mathrm{i}}/s_{\mathrm{r}}$ (via $\omega_n r_{\mathrm{i}}$).

4.1.2 Isotropic Bars - Steel Bar Case

Based on the *Case II* solutions (section 3.2.2) and Equation (40), the elastic modulus due to a steel bar is

$$\hat{D}^{\mathrm{e}}_{\mathrm{bar}} = \left(\sum_{n=1}^{\infty} \frac{\alpha_n^2 \zeta_n}{\alpha_0^2 E_{\mathrm{s}}} \right)^{-1} \tag{46}$$

where ζ_n is dimensionless and given by

$$\zeta_n = \left(1 - \nu_{\mathrm{s}}^2\right) J_1^2(\omega_n r_{\mathrm{i}}) / F_n \tag{47}$$

E_{s} and ν_{s} are Young's modulus and Poisson's ratio, respectively, for steel, and F_n is given by Equation (38) with ν_{s} substituted for ν. The radial elastic modulus accounting for both contributions can then be written as

$$\hat{D}^{\mathrm{e}} = \left[\sum_{n=1}^{\infty} \frac{\alpha_n^2}{\alpha_0^2} \left(\frac{\zeta_n}{E_{\mathrm{s}}} - \frac{\kappa_n}{E_{\mathrm{c}}} \right) \right]^{-1} \tag{48}$$

4.2 Results

The above analytical results will now be applied to three bond specimens for FRP bars (Table 1). The calculated radial elastic moduli of the FRP-concrete interfaces and the "transverse stiffness" (Equation 19) of the bar are listed in Table 2. Specimen "a" corresponds to the bond specimen of Malvar [18,19] using the "type D" GFRP bar. The bar has a helical surface, and a relatively concentrated interface contact ($L_{\mathrm{t}}/s_{\mathrm{r}}$=1/8) is assumed. Such concentrated contact is possible since the surface misfit between the bar and concrete can be significant when relative slip occurs. Specimen "b" corresponds to the bond specimen of Bakis *et al*. [21]. The CFRP bar has machined lugs with a square cross-section, and the contact length L_{t} is assumed to be the lug width. Specimen "c" corresponds to some recent bond tests of a CFRP bar (manufactured by Marshall Industry) in light weight concrete. The ribs are similar to those of a steel bar, and the contact length used for this bar is close to the rib width. Two types of concrete are used in the specimen models: normal strength and light weight. For our examples, the light weight concrete has a lower Young's modulus but higher tensile strength than the normal strength concrete. The ratio $r_{\mathrm{o}}/r_{\mathrm{i}}$ verifies the assumption that the hollow cylinder of concrete is "sufficiently thick" for the previous solution [1] to be applicable (section 4.1). A half-cosine distribution of traction over L_{t} is assumed in the calculations leading to Table 2.

It is well known that the "transverse stiffness" of an FRP bar ($\hat{D}^{T}_{bar}$) is significantly less than that of a steel bar. The results show that (for the values of L_t considered) reduced contact produces almost twice as much radial compliance ($1/\hat{D}^{e}$) as that associated with a uniform radial deformation ($1/\hat{D}^{T}_{bar}$). The combined radial compliance promotes the behavior shown in Figure 1.

We identified (section 4.1.1) three factors that affect $\hat{D}^{e}$: (1) traction distribution, (2) material constants, and (3) r_i/s_r. Parameter studies addressing these three factors are presented in the next three sub-sections. The effects of the individual length parameters L_t, r_i and s_r are not studied separately, but they can be inferred from the effects of L_t/s_r and r_i/s_r ratios.

4.2.1 Effect of Traction Distribution on $\hat{D}^{e}$

We consider three types of traction distributions: uniform, half-cosine and triangular (Table 3). The traction distribution affects the radial elastic modulus of the interface (for brevity, *elastic modulus*) via the term α_n/α_0. The expressions in Table 3 indicate that the "nondimensionalized contact length" ($\beta=L_t/s_r$) and the shape of the traction distribution (*distribution type*) affect the concentration of the traction. For the same distribution type, the traction is more concentrated for a smaller β; whereas for the same value of β, the traction is most concentrated for the triangular distribution and least for the uniform distribution.

The effect of the traction distribution is examined in Figure 4. $\hat{D}^{e}/E_c$ *vs.* L_t/s_r (β) is plotted for three types of distributions and the three specimens defined in Table 1. An increased concentration of the traction (either due to distribution type or β) produces a more compliant interface; i.e., for a fixed distribution type, $\hat{D}^{e}$ decreases with β, and for a fixed β, $\hat{D}^{e}$ decreases with the more concentrated distribution type. In some applications, the contact length may be estimated but the actual traction distribution is generally unknown. The results indicate that as β decreases the effect of the distribution upon the elastic modulus decreases. This effect is most pronounced in comparing the two non-uniform distributions, which give very close predictions for a large range of β. For full-contact ($\beta=1$) the elastic modulus becomes infinite for the uniform traction case, since the traction distributions of the rib-scale and bar-scale models are the same; any other traction distribution representing full-contact will yield a finite elastic modulus for the interface.

4.2.2 Effects of Material Constants on $\hat{D}^{e}$

In the previous study [1] Cox and Yu [1999] the deformation of the reinforcing element was neglected. This idealization was assumed to be valid for the example problem of a steel bar in a concrete matrix. First this assumption is evaluated using the solution for the deformation of the bar. Figure 5(a) shows the constituent contributions to $\hat{D}^{e}$ by steel, concrete and FRP for the Malvar specimen (specimen "a"). The steel bar is assumed to have the same configuration as the GFRP bar. The material properties of the steel bar are assumed to be E_s=190 GPa and ν_s=0.3. The half-cosine traction distribution is used in the calculations. The elastic modulus associated with local deformation of the steel bar is much higher than that due to local deformation of concrete or FRP. Figure 5(b) validates the previous assumption [1] Cox and Yu [1999] since the elastic compliance of the steel-concrete interface is only slightly more than that associated with the concrete alone. In contrast, the FRP-concrete interface is much more compliant reflecting the importance of the transverse compliance of the FRP bar.

Figure 6 contains the results of a parametric study on the effects that the seven independent material constants have on $\hat{D}^{e}$. Percent changes in $\hat{D}^{e}$ *vs.* percent changes in each material

constant are shown for each of the three specimens. A half-cosine distribution of traction was assumed in the calculations. The main trends are summarized as follows:

1. Changes in E_L, ν_{LT} and ν_c have the least effects on $\hat{D}^e$ for all of the specimens; ±10% changes in these parameters lead to negligible changes in $\hat{D}^e$. Changes in ν_{TT} and μ_{LT} do not have the largest effects on $\hat{D}^e$ for any of the specimens but do produce relatively significant changes in $\hat{D}^e$.
2. For interfaces between FRP and normal strength concrete (Figures 6a,b), changes in E_T have the most significant effect on $\hat{D}^e$, whereas changes in E_c have significant but less pronounced effects.
3. For the interface between FRP and light weight concrete (Figure 6c), both E_T and E_c have the most significant effects on $\hat{D}^e$, due to the reduced E_c of light weight concrete.

4.2.3 Effects of r_i/s_r on $\hat{D}^e$ and D^e

The parameter r_i/s_r (bar radius / rib spacing) affects $\hat{D}^e$ through the argument of the Modified Bessel functions. Figure 7 shows the effect of r_i/s_r upon $\hat{D}^e/E_c$ for the three bond specimens. The variation in the elastic modulus and of the constituent contributions ($\hat{D}^e_{bar}$ and $\hat{D}^e_{con}$) is shown. Again a half-cosine traction distribution is assumed. The parameters are given in Table 1 except that r_i varies while s_r is held fixed. The range of r_i/s_r is set to (0,0.56] for the Malvar specimen to maintain a sufficiently large r_o/r_i ratio (Figure 7a) and is set to (0,1] for the other two specimens (Figures 7b,c). The main trends are summarized as follows:

1. The elastic modulus decreases as the r_i/s_r ratio decreases; however, the variation in the FRP contribution becomes very small when r_i/s_r is relatively small.
2. The effect of the FRP upon the elastic compliance is greater than that of the concrete, and their difference is more significant for the normal strength concrete-FRP interfaces (Figures 7a,b) than for the light weight concrete-FRP interface (Figure 7c). In all cases the difference in the two contributions decreases as r_i/s_r decreases.

$\hat{D}^e$ was defined as the elastic modulus relating σ and q_n. As an alternative description of the elastic response, the interface stiffness (D^e) relates σ and δ_n (Equation 3a). The difference in $\hat{D}^e$ and D^e is a factor of $1/d_b$. When d_b (or r_i) is constant, the variation in $\hat{D}^e$ also implies the variation in D^e (sections 4.2.1 and 4.2.2). The variation of D^e with r_i/s_r for the same three specimens is shown in Figure 8. The factor $1/d_b$ causes D^e to be unbounded as r_i approaches zero. While the second conclusion drawn above for $\hat{D}^e$ still holds for D^e, the first conclusion is no longer true. For large r_i/s_r ratios, D^e increases slightly with decreasing r_i/s_r; whereas, for sufficiently small r_i/s_r ratios, D^e increases dramatically with decreasing r_i/s_r.

5. APPLICATION

The mechanical interaction between FRP bars and concrete provides a good application area for the developed theory. For larger scale (bar-scale) modeling, we seek to homogenize the traction distribution and account for the local elastic deformation through the radial elastic modulus. However, the concrete does not always behave linear elasticly since compressive, radial interface tractions (e.g., due to mechanical interlocking) can be large enough to split the adjacent concrete longitudinally. Figure 9 shows the end-view of a specimen having three longitudinal cracks. The ability of the elastic modulus to represent the effects of reduced contact when significant longitudinal cracking occurs, and the importance of the reduced contact on the radial response are examined in this section.

Again we examine the bond specimens described in Table 1. Not all the bond specimens failed in splitting in the actual tests, but they still provide useful examples to evaluate the effect of the elastic modulus upon the cracking behavior. Axisymmetric finite element models are adopted for these specimens. Again the FRP is idealized as being transversely isotropic and linear elastic. The concrete is modeled as quasibrittle, with longitudinal cracks modeled as *cohesive cracks*(Hillerborg *et al.* [1976]) [22] using the approach of Rots [23] for axisymmetric FE models. Each crack is idealized as being planar with a process zone of infinitesimal thickness and finite length. The cohesive stress (σ_{cr}) bridging the cracked surfaces is related to the crack opening (w) via the following relationship(Reinhardt et al. ~85) [24] (Figure 10)

$$\sigma_{cr} = f_t\left[\left(1+c_1\hat{w}^3\right)e^{-c_2\hat{w}} - \left(1+c_1\right)\hat{w}e^{-c_2}\right] \tag{49}$$

where $\hat{w}$ is the ratio of w to the critical crack opening,w_0[1], f_t is the tensile strength of concrete, and c_1 and c_2 are model parameters. The fracture energy G_f is defined as the energy required to create unit areas of fractured surfaces (i.e., the area under the σ_{cr}-w curve). Typical values of f_t, G_f, w_0, c_1 and c_2 for normal strength and light weight concrete are listed in Table 4. Three longitudinal cracks are assumed and the concrete material between the cracks is assumed to behave linear elasticly.

To examine the effect of using the elastic modulus, axisymmetric FE models of unit cells of all three bond specimens were developed at both scales – the rib- and bar-scales (Figure 2). The case of a uniformly distributed t over L_t is examined, thus the rib-scale model is referred to as being "ring-loaded." The "bar-scale" or homogenized model incorporates a homogenized traction and an interface with a stiffness D^e defined by Equations (3b) and (45). Figure 11 shows the axisymmetric FE meshes for the ring-loaded models with enlargements of the loaded regions. Using symmetry only half of the unit cell is modeled, and roller boundary conditions are applied along the r-axis. The homogenized models use meshes that are uniformly graded in the z-direction, but more finely graded near the interface in the r-direction.

The "interface responses" of the two types of models are compared in Figure 12 for all of the specimens. The magnitude of σ (t L_t/s_r for the ring-loaded models) *vs*. Δu is compared for each of the constituent materials and their combination. Δu is the work conjugate average displacement (or relative displacement) corresponding to the loading; e.g., for concrete Δu is the average $u_r(r_i)$ over L_t (where L_t=s_r for the homogenized models) while for the concrete-FRP combination it is the average interface separation over L_t. Figure 13 examines the response of Malvar's type D specimen for contact ratios (L_t/s_r) of: 1, 1/2, 1/4, and 1/8. The main observations are:

1. For all of the specimens, the responses of both types of models are nearly indistinguishable for the concrete, FRP and their combination.
2. All of the specimens examined exhibited snap-back behavior in the radial response. The added compliance of the FRP increases the amount of elastic strain energy stored at the peak load and the potential of snap-back behavior in the radial response.
3. The effect of FRP compliance is less pronounced for the specimen having light weight concrete since $1/D^e_{con}$ due to the light weight concrete is more comparable to $1/D^e_{bar}$ due to the FRP.
4. The potential for snap-back behavior increases with a reduction in the contact area because of the increased elastic energy stored in local deformation.

The predicted snap-back behavior is important in this application for both physical and computational reasons. From a physical point of view, it suggests that concrete splitting failures produced by the loading of FRP bars may have a more "explosive nature". From a computational point of view, this severe instability can be difficult to follow when simulating

[1] The smallest crack opening for which σ_{cr}=0.

bond behavior, because the needed radial contraction to follow the snap-back response (in a quasi-static analysis) may not be readily controlled in many pull-out type tests.

6. SUMMARY AND CONCLUSIONS

By accounting for "static equivalence" and "energy equivalence" the radial elastic response due to a known traction distribution along an interface (e.g., attributed to mechanical interlocking) can be accurately represented in a larger scale (i.e., homogenized) model. The actual traction distribution causes deformation of each constituent material which can be represented by additional interface compliance in the homogenized model. By making several simplifying assumptions and adopting a unit cell approach, expressions for the radial elastic modulus can be obtained in closed form. The analytical expression for the elastic modulus reflects its dependence upon the traction distribution, material properties, and bar geometry.

The theoretical development of the radial elastic modulus is applicable to the problem of the mechanical interaction between FRP bars and concrete. The homogenized model (or "bar-scale" for this application) incorporates a radial elastic modulus that is very important toward predicting the longitudinal cracking in the adjacent concrete. To study the effects of traction distribution, material properties, and bar geometry on the radial elastic modulus for FRP bars in a concrete matrix, three bond specimens are examined. Among the findings were:

1. An increased concentration of the traction (either due to distribution type or contact length) produces a more compliant interface. As the nondimensionalized contact length (β) decreases the effect of the distribution type upon the radial elastic modulus decreases. Even for full-contact the radial elastic modulus is finite except for the case of a uniform traction distribution.
2. Changes in E_L, ν_{LT} and ν_c have negligible effects on the variation of $\hat{D}^e$, while changes in the other four material properties have a significant effect upon $\hat{D}^e$. $\hat{D}^e$ is most sensitive to changes in (i) E_T for normal strength concrete and (ii) E_T and E_c for light weight concrete.
3. The ratio of bar radius to rib spacing (r_i/s_r) affects the elastic modulus ($\hat{D}^e$) and the elastic stiffness (D^e) differently. Reducing the r_i/s_r ratio leads to a decreased elastic modulus and increased stiffness of the interface.

The same three bond specimens were used to examine how $\hat{D}^e$ affects the radial response (measured "at the interface") when the concrete develops longitudinal cracking. The homogenized model (bar-scale) was compared to a model with the actual traction distribution (rib-scale), and among the findings were:

1. For all of the specimens, the responses of both types of models are nearly indistinguishable for the concrete, FRP and their combination.
2. Snap-back behavior occurred for all of the specimens, in part due to the elastic energy associated with local deformation. For normal strength concrete the local deformation of the FRP was more significant, but for light weight concrete the local deformation of the concrete was equally significant.

The actual interface traction distributions are generally unknown, but the results do provide additional insight into the behavior resulting from the mechanical interaction between FRP bars and concrete. The results indicate that the contact conditions may have a significant effect upon the radial response, and the analysis provides data on an elastic modulus that accurately characterizes the effect of the interface traction state even when the concrete exhibits longitudinal cracking.

ACKNOWLEDGMENTS

Support for this study by the National Science Foundation (grant no. CMS-9872609), Naval Facilities Engineering Service Center (contract no. N0024499P2444), and the Office of Naval Research is gratefully acknowledged.

REFERENCES

1. Cox, J.V. and H. Yu. 1999. "A Micromechanical Analysis of the Radial Elastic Response associated with Slender Reinforcing Elements within a Matrix," *Journal of Composite Materials*, 33(23):2161-2192.
2. Goodman, R.E., R.L. Taylor and T.L. Brekke. 1968. "A Model for the Mechanics of Jointed Rock," *Journal of Soil Mechanics and Foundation Division*, ASCE, 94(SM3): 637-659.
3. Ko, C.-C., D.H. Kohn, and S.J. Hollister. 1996. "Effective Anisotropic Elastic Constants of Bimaterial Interphases: Comparison Between Experimental and Analytical Techniques," *Journal of Materials Science–Materials in Medicine*, 7(2):109-117.
4. Nevard, J. and J.B. Keller. 1997. "Homogenization of Rough Boundaries and Interfaces," *SIAM Journal of Applied Mathematics*, 57(6):1660-1686.
5. Aboudi, J. 1987. "Damage in Composites Modeling of Imperfect Bonding," *Composites Science and Technology*, 228:103-128.
6. Achenbach, J.D. and H. Zhu. 1990. "Effect of Interphases on Micro and Macromechanical Behavior of Hexagonal-Array Fiber Composites," *Journal of Applied Mechanics*, 57:956-963.
7. Benveniste, Y. 1985. "The Effective Mechanical Behavior of Composite Materials with Imperfect Contact Between the Constituents," *Mech. Mater.*, 4:197-208.
8. Hashin, Z. 1990. "Thermoelastic Properties of Fiber Composites with Imperfect Interfaces," *Mech. Mater.*, 8:333-348.
9. Theocaris, P.S., E.P. Sideridis, and G.C. Papanicolaou. 1985. "The Elastic Longitudinal Modulus and Poisson's Ratio of Fiber Composites," *Journal of Reinforced Plastics and Composites*, 4:396-418.
10. Jayaraman, K., K.L. Reifsnider, and R.E. Swain. 1993. "Elastic and Thermal Effects in the Interphase: Part II. Comments on Modeling Studies," *Journal of Composites Technology and Research (JCTRER)*, 151(1):3-13.
11. Tepfers, R. 1979. "Cracking of Concrete Cover along Anchored Deformed Reinforcing Bars," *Magazine of Concrete Research*, 31(106):3-12.
12. Benmokrane, B., B. Tighiouart, and O. Chaallal. 1996. "Bond Strength and Load Distribution of Composite GFRP Reinforcing Bars in Concrete," *ACI Materials Journal*, 93(3):246-253.
13. Cox, J.V. and L.R. Herrmann. 1998. "Development of A Plasticity Bond Model for Reinforced Concrete," *Mechanics of Cohesive-frictional Materials*, John Wiley and Sons, 3:155-180.
14. Guo, J. and J.V. Cox. 2000. "An Interface Model for the Mechanical Interaction between FRP Bars and Concrete," *Journal of Reinforced Plastics and Composites*, 19(1):15-33.
15. Cox, J.V. and J. Guo. 1999. "Modeling the Stress State Dependency of the Bond Behavior of FRP Tendons," ACI Special Publication, *Fourth International Symposium on FRP Reinforcement for RC Structures*, Baltimore.
16. Needleman, A. 1992. "Micromechanical Modeling of Interfacial Decohesion," *Ultrmicroscopy*, 40:203-214.
17. Lurie, S.A. and V.V. Vasiliev. 1995. *The Biharmonic Problem in the Theory of Elasticity*, Amsterdam: Gordon and Breach Science Publishers.
18. Malvar, L.J. 1994. "Bond Stress-Slip Characteristics of FRP Rebars," *Technical Report TR-2013-SHR*, Naval Facilities Engineering Service Center.
19. Malvar, L.J. 1995. "Tensile and Bond Properties of GFRP Reinforcing Bars," *ACI Materials Journal*, 92(3):276-285.
20. Hashin, Z. 1983. "Analysis of Composite Materials - A Survey," *Journal of Applied Mechanics*, 50: 481-505.
21. Bakis, C.E., V.S. Uppuluri, A. Nanni, and T.E. Boothby. 1998. "Analysis of Bonding Mechanisms of Smooth and Lugged FRP Rods Embedded in Concrete," *Composites Science and Technology*, 58: 1307-1319.

22. Hillerborg, A., M. Modéer, and P.A. Petersson. 1976. “Analysis of Crack Formation and Crack Growth in Concrete by Means of Fracture Mechanics and Finite Elements,” *Cement and Concrete Research*, 6:773-782.
23. Rots, J.G. 1988. *Computational Modeling of Concrete fracture*, Dissertation, Department of Civil Engineering, Delft University of Technology, Delft, the Netherlands.
24. Reinhardt, H.W., H.A.W. Cornelissen, and D.A. Hordijk. 1986. “Tensile Tests and Failure Analysis of Concrete,” *Journal of the Structures Division*, ASCE, 112(11):2462-2477.

Table 1. Specimen data.

Specimen	E_L GPa	E_T GPa	μ_{LT} GPa	ν_{LT}	ν_{TT}	E_c GPa	ν_c
a	39.8	9.29	3.78	0.274	0.42	30.7	0.17
b	116.6	7.51	3.74	0.272	0.31	31.5	0.2
c	119.5	7.55	4.0	0.294	0.45	15.7	0.17

Specimen	L_t mm	r_i mm	s_r mm	L_t/s_r	r_i/s_r	r_o/r_i
a	4.29	9.525	34.3	0.125	0.28	4.0
b	3.8	6.35	12.7	0.3	0.5	13.5
c	2.29	5.08	7.62	0.3	0.67	$\geq$7.5

a - Malvar's type D GFRP bar and normal strength concrete;
b - Bakis et al. [21], CFRP bar and normal strength concrete;
c - Marshall CFRP bar and light weight concrete.

Table 2. Elastic moduli of FRP-concrete interfaces.

Specimen	$\hat{D}^e_{bar}$ GPa	$\hat{D}^e_{con}$ GPa	$\hat{D}^e$ GPa	$\hat{D}^e/E_c$	$\hat{D}^T_{bar}$ GPa	$\hat{D}^T_{bar}/E_c$
a	6.52	18.3	4.81	0.16	34.1	1.11
b	14.3	54.3	11.3	0.36	22.1	0.70
c	21.3	34.2	13.1	0.84	28.0	1.78

Table 3. Classification of traction distributions.

Distribution Type		t	α_0	α_n
uniform	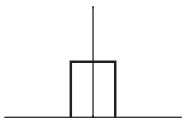	$\frac{s_r}{L_t}$, $z\in[-L_t/2, L_t/2]$	$\sqrt{s_r}$	$\sqrt{2s_r}\left[\frac{\sin(n\beta\pi)}{n\beta\pi}\right]$, $\beta=L_t/s_r$
half-cosine	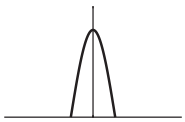	$\frac{\pi s_r}{2L_t}\cos\left(\frac{\pi z}{L_t}\right)$, $z\in[-L_t/2, L_t/2]$	$\sqrt{s_r}$	$\sqrt{2s_r}\left[\frac{\cos(n\beta\pi)}{1-4n^2\beta^2}\right]$, if $2n\beta\neq 1$; $\sqrt{2s_r}\left(\frac{\pi}{4}\right)$, if $2n\beta=1$.
triangular	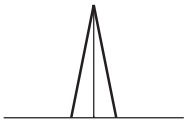	$\frac{2s_r}{L_t}\left(1+\frac{2z}{L_t}\right)$, $z\in[-L_t/2, 0]$; $\frac{2s_r}{L_t}\left(1-\frac{2z}{L_t}\right)$, $z\in(0, L_t/2]$.	$\sqrt{s_r}$	$\sqrt{2s_r}\left[\frac{\sin(n\beta\pi/2)}{n\beta\pi/2}\right]^2$

Note: The listed magnitudes of t correspond to σ=1. The dimensions of t are force/length^2, and the dimensions of the α's are force/length$^{3/2}$.

Table 4. Typical fracture parameters for concrete.

Concrete Type	f_t MPa	G_f J/m^2	w_0 mm	c_1	c_2
normal strength	2.79	100	0.2	18.8	6.93
light weight	3.18	100	0.1	3.56	2.0

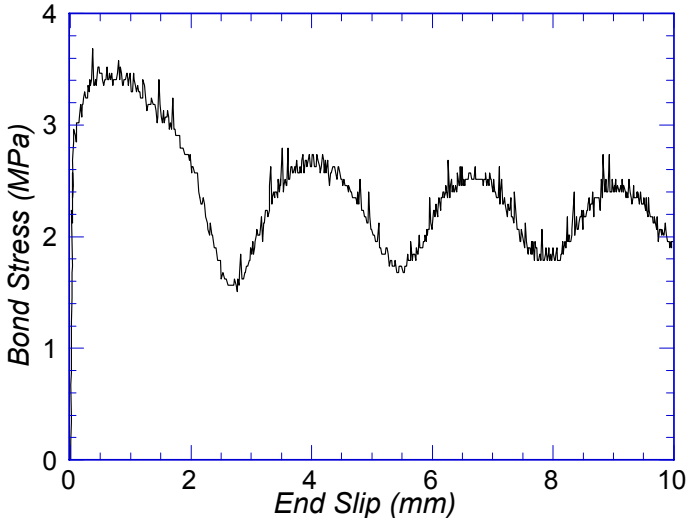

Figure 1. *Bond stress vs. slip for a CFRP bar.*

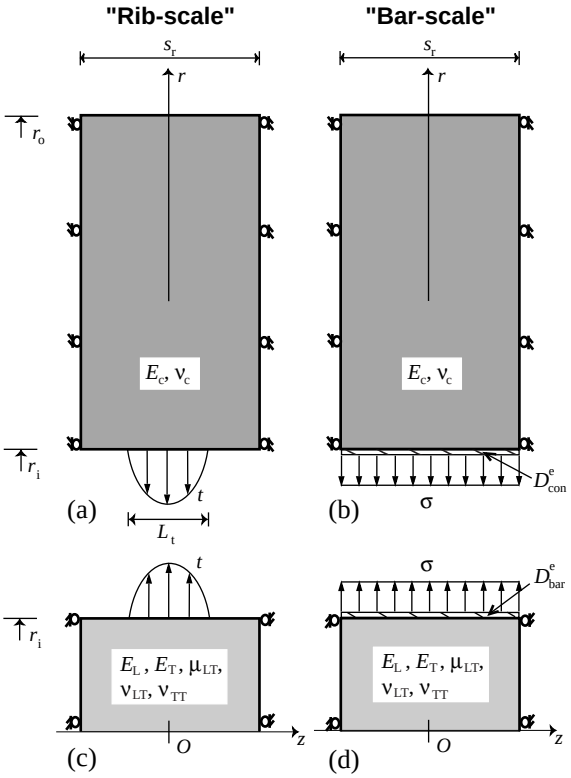

Figure 2. *Idealized analytical models.*

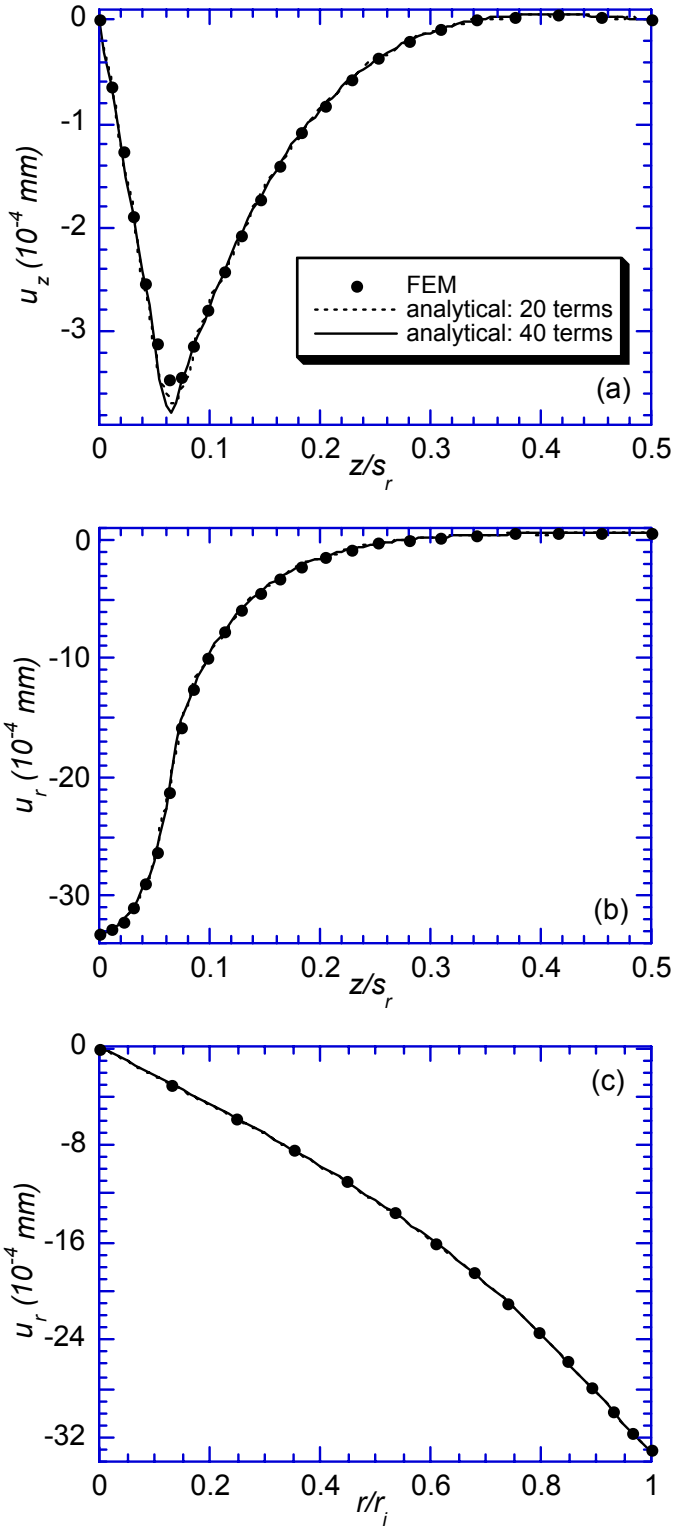

Figure 3. *Analytical vs. FE solutions for Malvar's type D GFRP bar: (a) u_z along $r=r_i$, (b) u_r along $r=r_i$, and (c) u_r along $z=0$.*

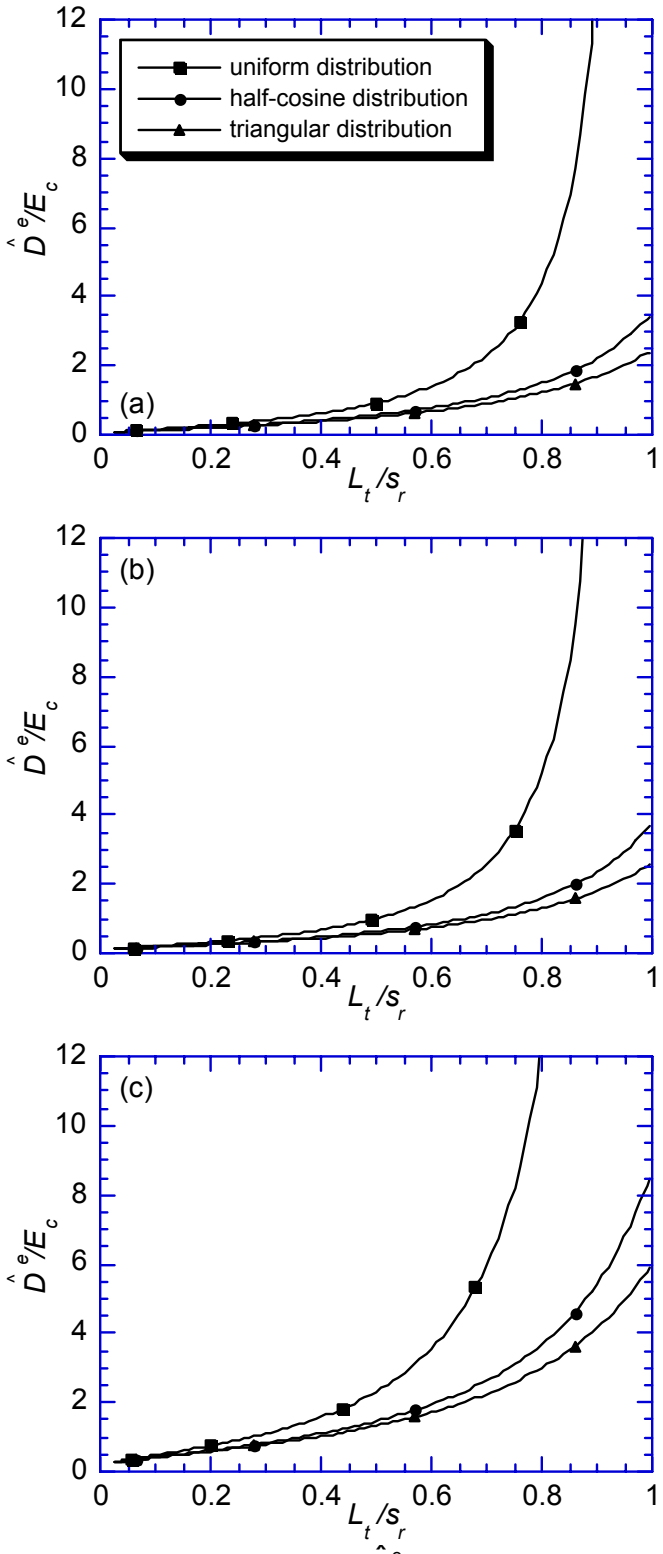

Figure 4. *Dependence of $\hat{D}^e$ on contact length and traction distribution type for (a) Malvar's type D specimen, (b) specimen of Bakis et al. [21], and (c) Marshall specimen.*

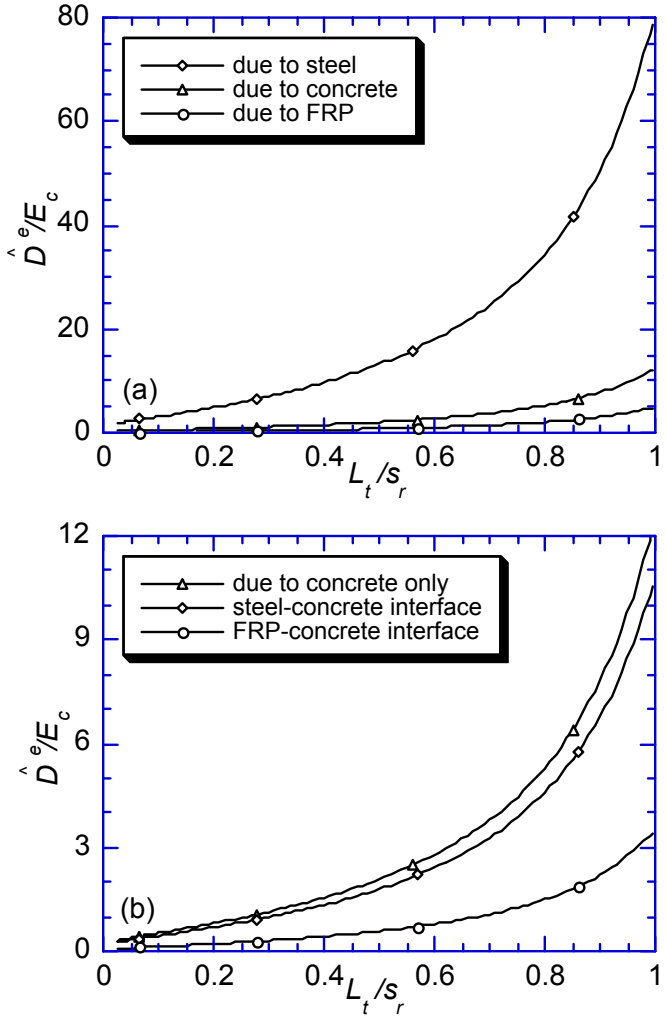

Figure 5. *Effect of constituent properties on $\hat{D}^e$ for Malvar specimen.*

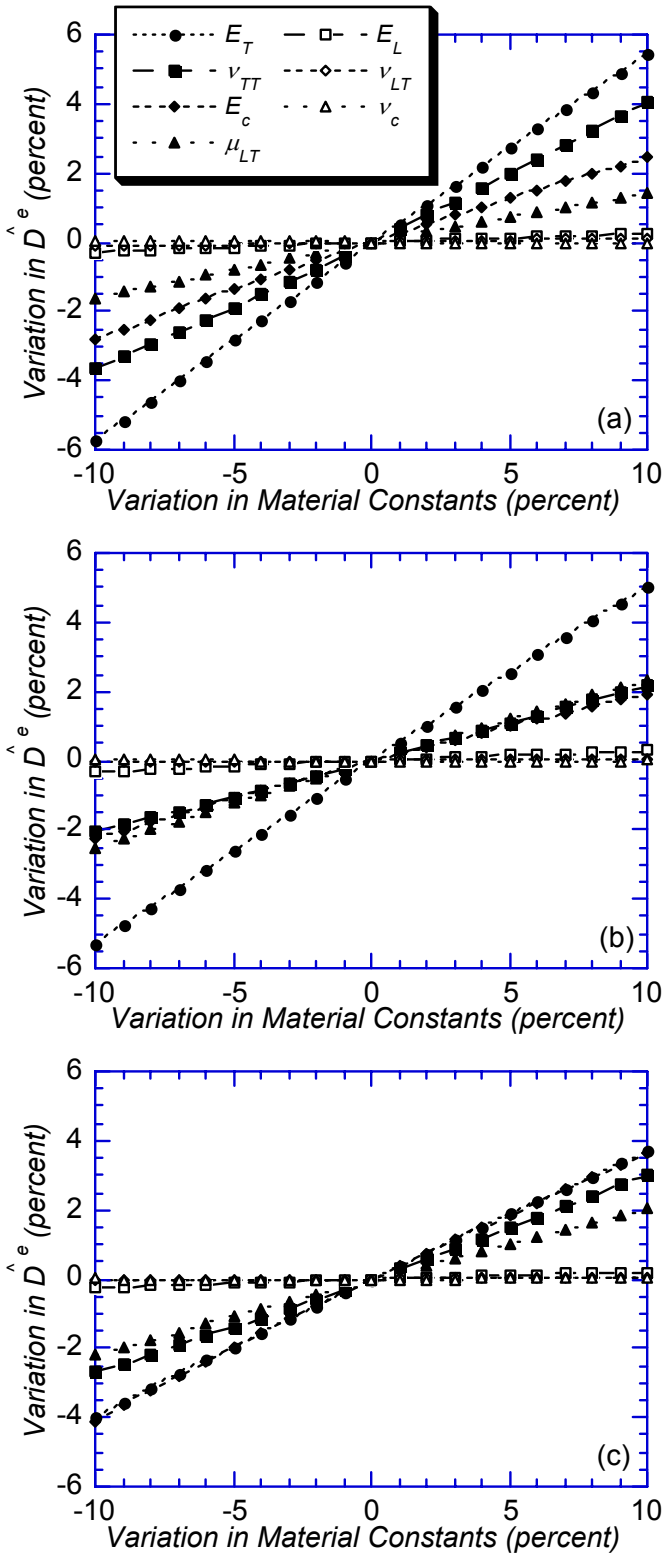

Figure 6. *Parametric studies of elastic constants for (a) Malvar's type D specimen, (b) specimen of Bakis et al. [21], and (c) Marshall specimen.*

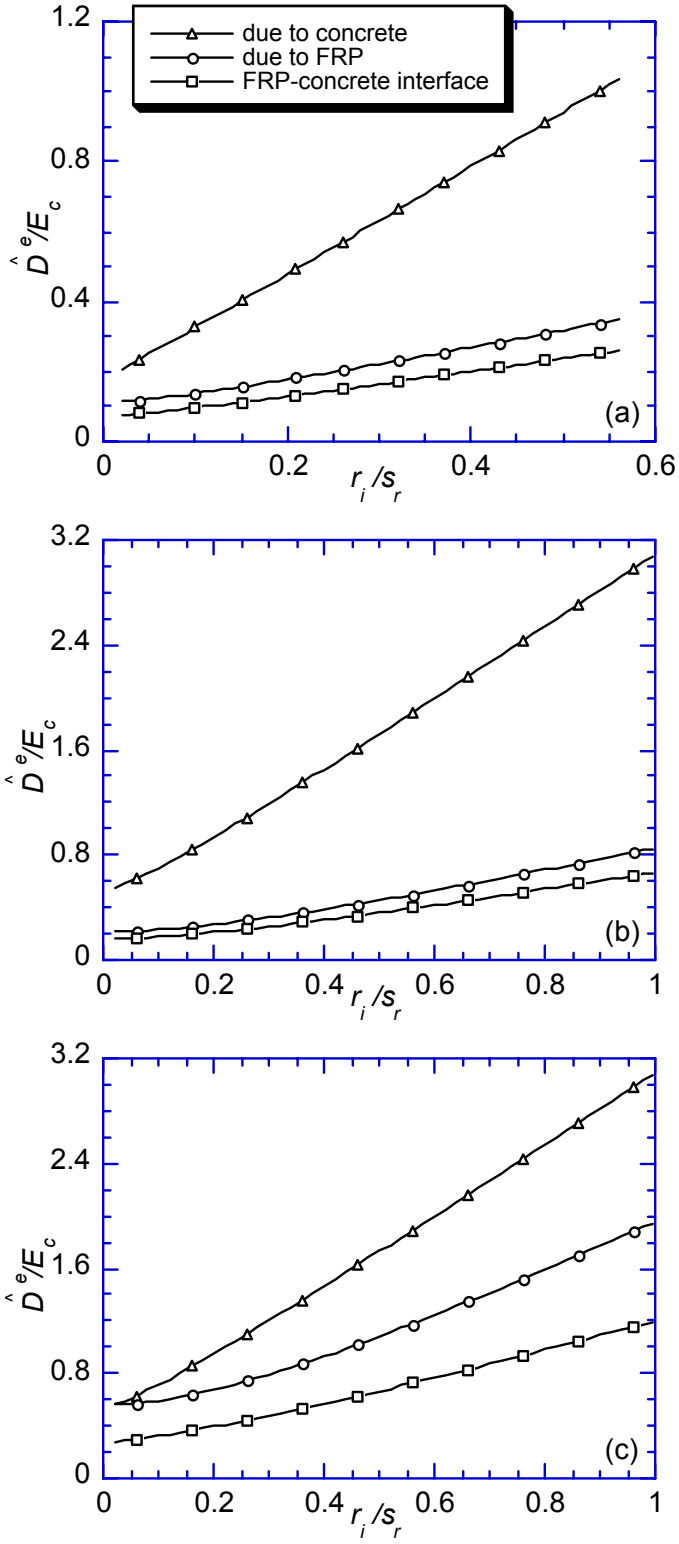

Figure 7. *Variation of elastic modulus with r_i/s_r for (a) Malvar's type D specimen, (b) specimen of Bakis et al. [21], and (c) Marshall specimen.*

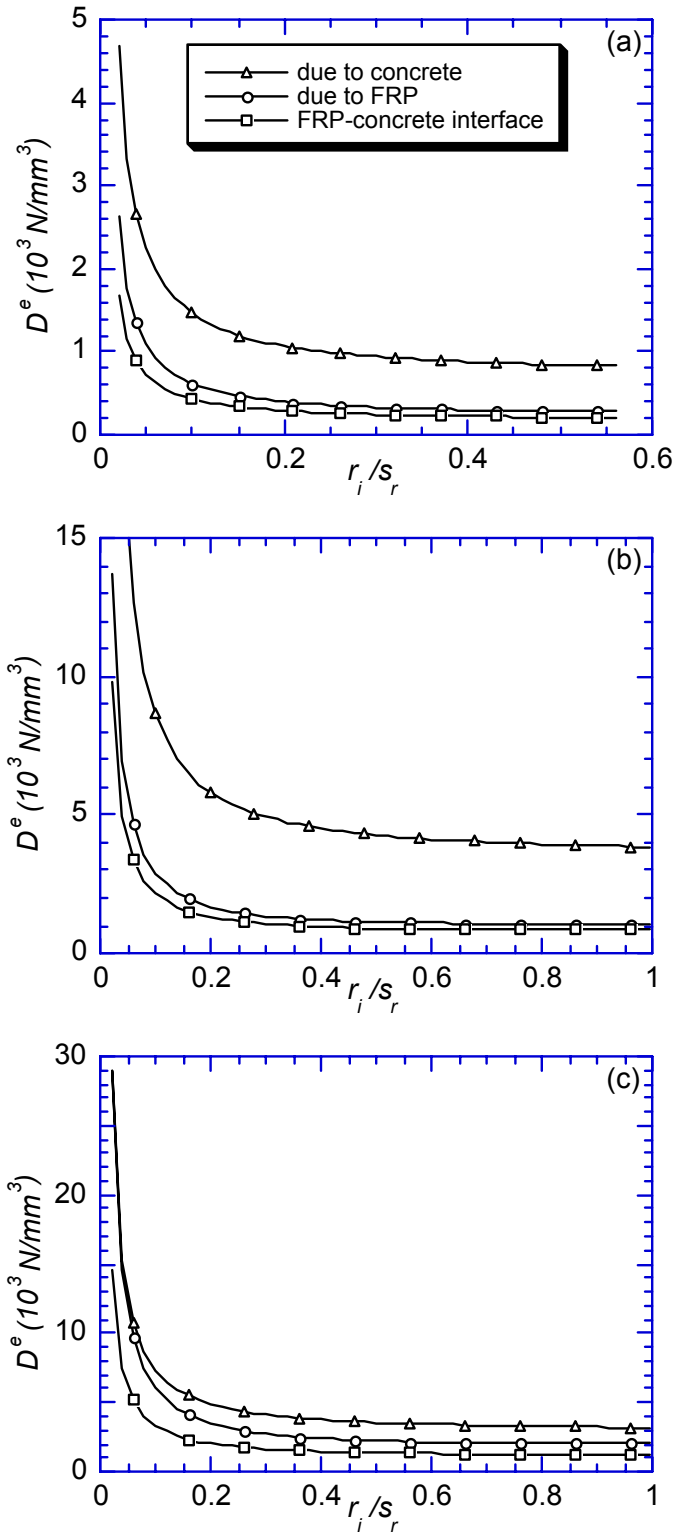

Figure 8. *Interface stiffness (D^e) vs. r_i/s_r for (a) Malvar's type D specimen, (b) specimen of Bakis et al. [21], and (c) Marshall specimen.*

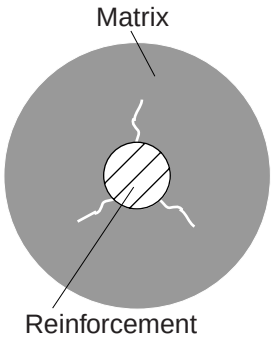

Figure 9. *Longitudinal cracks - end view.*

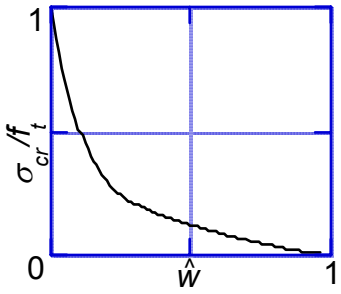

Figure 10. *Nondimensionalized cohesive stress-crack opening relationship.*

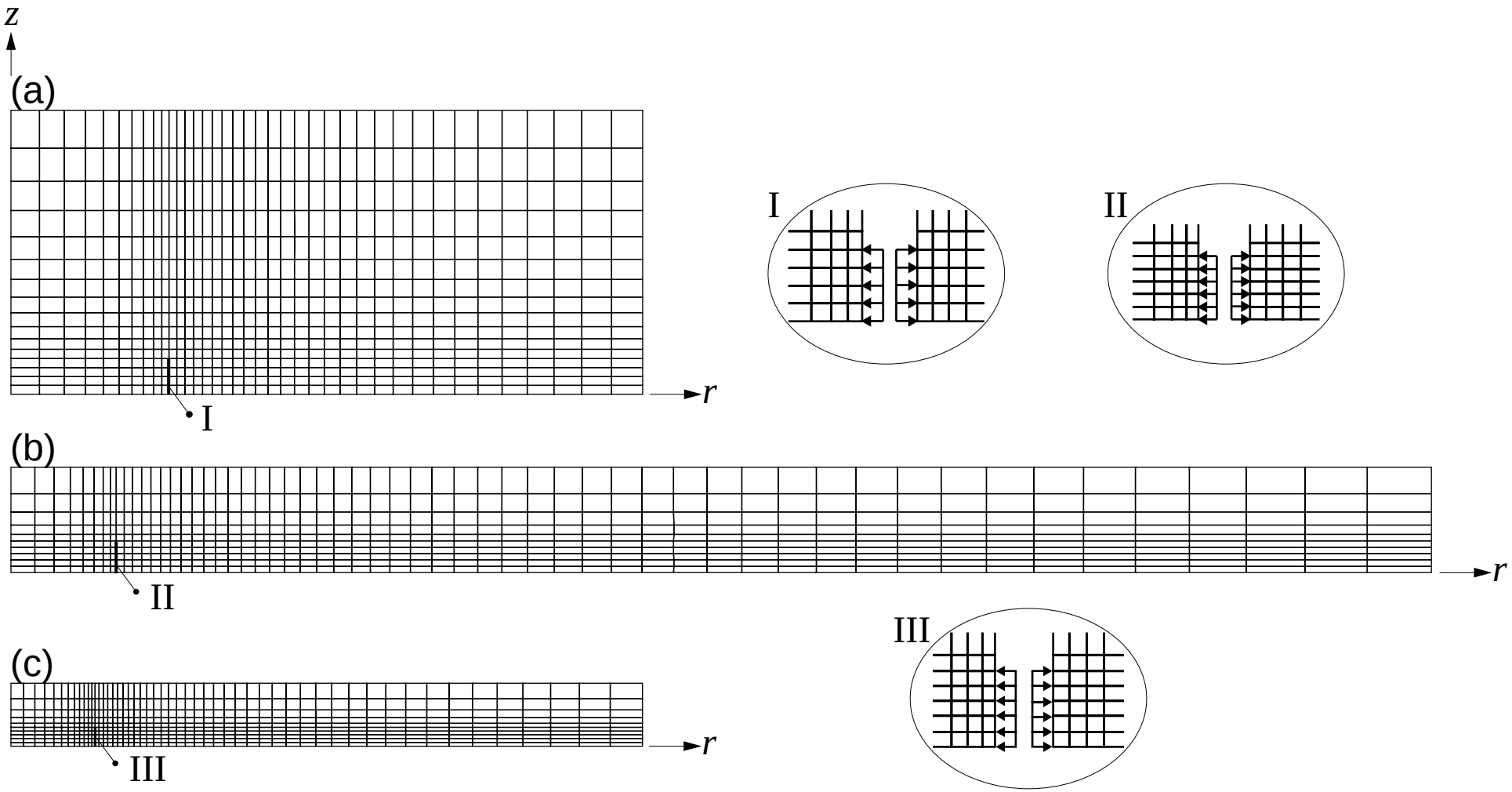

Figure 11. *Axisymmetric finite element meshes for ring-loaded specimens: (a) Malvar's type D specimen, (b) specimen of Bakis et al. [21], and (c) Marshall specimen. (Magnifications are 200% for I & II and 400% for III.)*

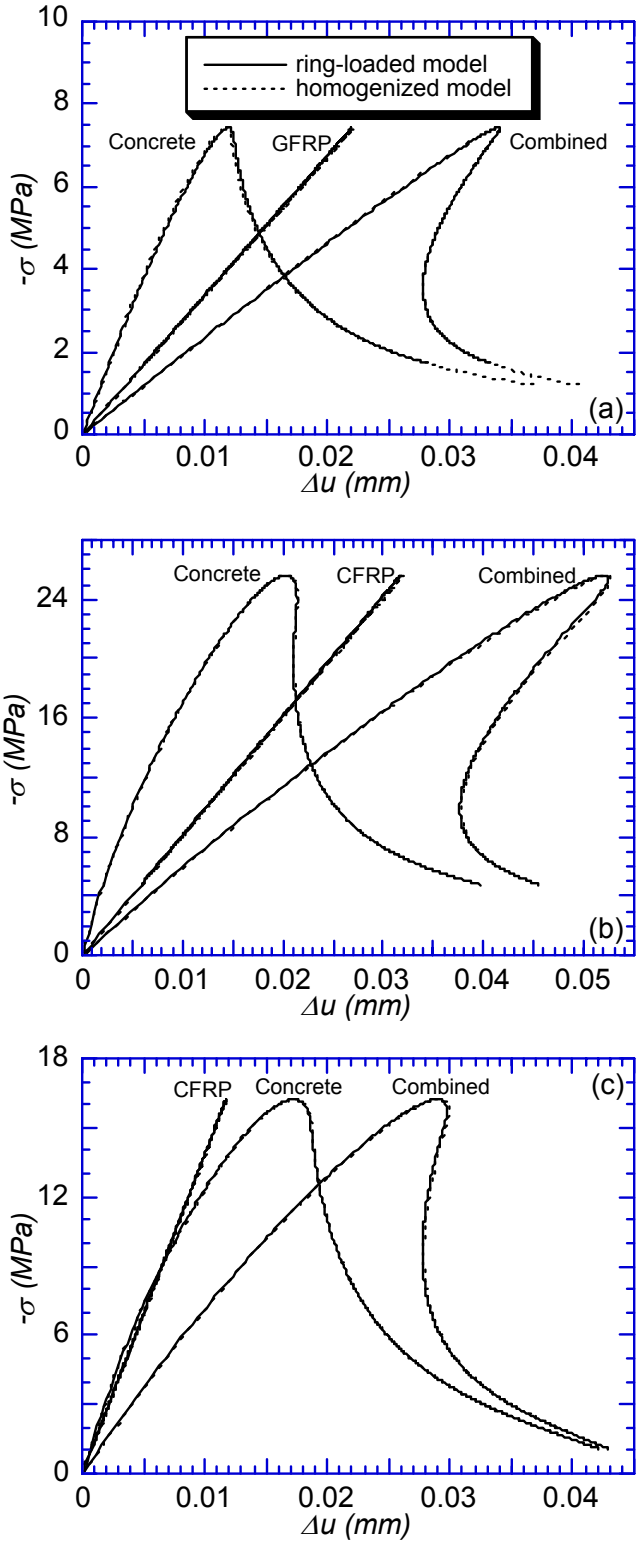

Figure 12. *Radial compression vs. interface separation for (a) Malvar's type D specimen, (b) specimen of Bakis et al. [21], and (c) Marshall specimen.*

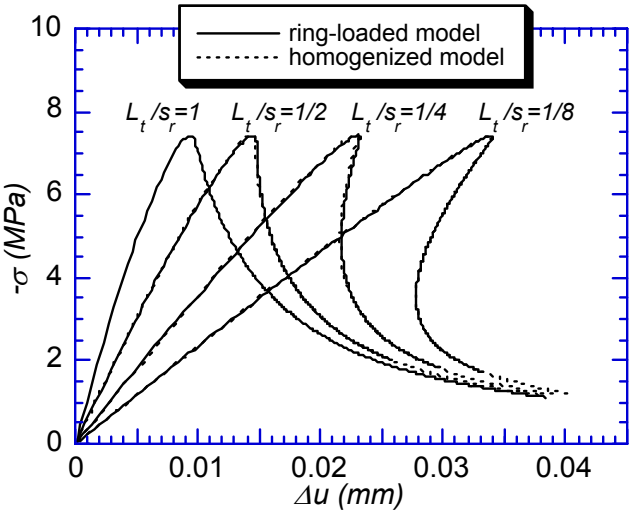

Figure 13. *Radial compression vs. interface separation for Malvar specimen under different contact conditions.*